

The 17th AIAA/ISSMO Multidisciplinary Analysis and Optimization Conference, 13 – 17 June 2016, Washington, D.C.

An Efficient Unsteady Aerodynamic and Aeroacoustic Design Framework Using Discrete Adjoint

Beckett Y. Zhou*, Tim Albring,[†] and Nicolas R. Gauger[‡]

Chair for Scientific Computing, TU Kaiserslautern

Bldg 34, Paul-Ehrlich-Strasse, 67663 Kaiserslautern, Germany

Carlos R. Ilario da Silva,[§] Thomas D. Economon,[¶] and Juan J. Alonso^{||}

Department of Aeronautics and Astronautics, Stanford University

Stanford, CA 94305, U.S.A.

In this paper, we present an unsteady aerodynamic and aeroacoustic optimization framework in which algorithmic differentiation (AD) is applied to the open-source multi-physics solver SU2 to obtain design sensitivities. An AD-based consistent discrete adjoint solver is developed which directly inherits the convergence properties of the primal flow solver due to the differentiation of the entire nonlinear fixed-point iterator. In addition, a coupled CFD-CAA far-field noise prediction framework using a permeable surface Ffowcs Williams-Hawkings approach in frequency domain is also developed. The resultant AD-based discrete adjoint solver is applied to both aerodynamic and aeroacoustic optimization problems. The results suggest that the unsteady adjoint information provided by this AD-based discrete adjoint framework is accurate and robust, due to the algorithmic differentiation of the entire design chain including the dynamic mesh movement routine and various turbulence model, as well as the hybrid CFD-CAA model. This study also shows the aerodynamic and noise design objectives to be mutually competing.

I. Introduction

The past several decades have seen significant progresses in the numerical methods for the design and optimization of aerospace systems. Since the advent of adjoint-based methods,^{1,2} for which the computational cost is independent of the number of design variables, researchers have been able to tackle many large-scale and practical problems, such as aerodynamic and aerostructural optimizations of complete aircraft configurations.^{3,4} In most applications, the underlying physical problem is considered to be in a steady state, as is evident from the rich body of literatures on the topic of aerodynamic shape optimization with steady Euler and Reynolds-averaged Navier-Stokes equations (RANS).

However, many aerospace problems are unsteady in nature, such as active flow control, turbomachinery, aeroelastic flutter, biologically-inspired flight and aeroacoustics. In comparison to the large strides made in its steady counterpart, unsteady adjoint-based optimization has not received as much attention and methods available to address such problem are consequently less mature. This has been primarily due to the need to store prohibitively large amount of solution data required to solve the unsteady adjoint equation. Furthermore, many unsteady problems involve moving aerodynamic surfaces. The need to accurately account for the requisite mesh movement in the governing equations and the accompanying adjoint equations introduces additional difficulties.

Nevertheless, with the growth of computing power and the improvement of time-accurate numerical methods, has led to more research effort in this area over the past decade. The renewed interest in reduction of aircraft noise – an inherently unsteady phenomenon, due to the ever-stringent aviation noise regulations, also served as a necessary catalyst. Rumpfkeil and Zingg developed a discrete adjoint formulation for unsteady aerodynamic shape optimization

*Ph.D. Candidate, Student Member AIAA, yuxiang.zhou@scicomp.uni-kl.de

[†]Ph.D. Candidate, tim.albring@scicomp.uni-kl.de

[‡]Professor, Senior Member AIAA, nicolas.gauger@scicomp.uni-kl.de

[§]Visiting Senior Research Associate, Associate Member AIAA, carlos.ilario@stanford.edu

[¶]Postdoctoral Scholar, Student Member AIAA, economon@stanford.edu

^{||}Professor, Associate Fellow AIAA, jjalonso@stanford.edu

and noise minimization based on 2D unsteady RANS (URANS),⁵ Mani and Mavriplis⁶ presented a discrete adjoint framework with deforming meshes for unsteady aerodynamic optimization of pitching airfoils. Nielsen and Diskin⁷ applied their discrete adjoint methodology with dynamic overset meshes to a large-scale complex helicopter configuration. Most recently, Economou et al.^{8,9} developed a continuous adjoint framework for unsteady aerodynamic and aeroacoustic optimization.

Under the discrete framework, the effort of the adjoint implementation can be eased by the use of algorithmic differentiation (AD), replacing the laborious and error-prone hand-differentiation of the discretized equations. This however, is not the only advantage of AD-based adjoint. By construction, AD-based adjoints are accurate to machine precision as they do not incur any roundoff or truncation error. In addition, the *frozen turbulence* assumption typically used in many URANS-based adjoint formulations is eliminated, since the turbulence models while not analytically differentiable are still *algorithmically* differentiable. The application of AD also leads to robust and consistent adjoints in that the adjoint solver inherits the same convergence properties as the primal solver. Lastly, if the operator overloading AD method is used with expression template technique in C++,¹⁰ the resultant discrete adjoint framework offers extra flexibility – the adjoint solver can be automatically updated with primal code modification and one can easily define any objective function from any state variable. This is an extremely attractive characteristic for unsteady optimization problems in the multidisciplinary setting using a suite of multi-physics solvers where the objective function may be different depending on the type of problems being addressed. AD-based discrete adjoint has been applied to steady aerodynamic shape design problems by Bischof et al.¹¹ and Gauger et al.¹² More recently, it was successfully applied by Nemeli et al.¹³ in the unsteady setting to the active flow control of an industry-relevant high-lift configuration HIREX from Airbus.

Noise reduction is another area where efficient unsteady simulation and optimization tools are necessary. The European Commission mandated in its report FLIGHTPATH2050 to reduce the perceived noise level by 65 percent from the level in 2000 by the year 2050. This corresponds to an ambitious reduction of 15dB. Similar goals have also been set by other regulatory bodies around the world. However, in a study conducted by Lockard and Lilley,¹⁴ it is revealed that even if all the noise sources from the high-lift systems and undercarriage are removed, the ‘clean’ configuration still falls short of such noise reduction goals. This means that designers must investigate innovative and unconventional ways to further improve the ‘clean configuration’ – the ‘lower bound’ must be reduced. The next generation aircraft will require innovative redesign of aerodynamic shapes and exploration of unconventional methods to meet the challenging noise reduction goals. Therefore, efficient and robust analysis and design tools well-suited for unsteady aerodynamic and aeroacoustic design problems are urgently needed.

It must be noted that the extension of an unsteady aerodynamic solver/optimizer to tackle computational aeroacoustic (CAA) problems is not a trivial one, as it gives rise to a multitude of challenges from both the simulation and optimization standpoints. From the simulation perspective, direct computation of noise typically leads to prohibitively large computational costs due to the disparate length and time scales that exist within the hydrodynamic and acoustic domains. Consequently, separate acoustic solvers need to be developed to handle the propagation of noise signals outside of the near-body source domain whose physics is resolved by a high-fidelity CFD solver. The aeroacoustic computations are typically carried out in a hybrid, multi-module fashion. In addition, specially tailored numerical treatments, such as low dissipation and dispersion schemes and non-reflective boundaries are required to accurately propagate the acoustic signals. A good review on the challenges of CAA has been presented by Colonius and Lele.¹⁵ From the design optimization perspective, the introduction of a new design objective/constraint – noise, complicates the optimization problem. Rumpfkeil and Zingg⁵ showed in their study that while the acoustic and aerodynamic design objectives do not appear to be *competing*, the noise-minimized and drag-minimized optimizations do not lead to the same optimal shape. Furthermore, in an experimental study presented by Herr et. al.,¹⁸ the noise-reducing porous material applied on the airfoil trailing-edges was shown to result in a marked loss of lift. Another open question is how to efficiently integrate the inherently unsteady CAA optimization tools, for noise minimization under low-speed landing and takeoff conditions in the aircraft design chain with the existing steady solver/optimizers developed for drag reduction under cruise conditions. These challenges can only be addressed with a ‘multi-objective’ and ‘multi-disciplinary’ mindset.

In this paper, we present the development of an AD-based discrete adjoint framework on an open source multi-physics suite SU2¹⁶ for applications to unsteady aerodynamic and aeroacoustic optimization problems. The remainder of the paper is organized as follows. In Section 2, the unsteady SU2 solver including a coupled CFD-CAA model using a permeable surface Ffowcs Williams-Hawkins (FW-H) approach as well as the optimization framework based on discrete adjoint and AD are presented. Section III presents validation results for the hybrid CFD-FWH far-field noise prediction framework as well as the coupled CFD-CAA adjoint. Optimization results are presented in Section IV while the conclusion and outlook for future work are outlined in Section V.

II. Unsteady Aerodynamic and Aeroacoustic Optimization Framework

II.A. Unsteady Multi-Physics Solver SU2

The Stanford University Unstructured (SU2) open source software suite was specifically developed for solving problems governed by partial differential equations (PDEs) and PDE-constrained optimization problems. It was developed with the aerodynamic shape optimization problems in mind. Therefore the suite is centered around a RANS solver capable of simulating compressible, turbulent flows commonly found in problems in aerospace engineering. The governing equations are spatially discretized using the finite volume method, on unstructured meshes. A number of convective fluxes discretization schemes have been implemented, such as the Jameson-Schmidt-Turkel (JST) scheme and the upwind Roe scheme. The turbulence can be either modeled by the Spalart-Allmaras(S-A) model or the Menter Shear Stress Transport (SST) Model. For unsteady flows, a dual time-stepping method can be used to obtain time-accurate solutions. SU2 suite has recently seen extensions in the multi-disciplinary setting such as the inclusion of a wave equation solver and a structural solver, making it well-suited for the unsteady multi-physics problems considered in this work.

For the sake of conciseness, details regarding the formulations and implementations of the SU2 solver suite will not be presented in this paper. Further details such as mesh deformation, dynamic mesh movement, multigrid implementations, validation and verification cases, as well as the continuous adjoint framework developed in tandem with SU2, the readers are referred to the published work by Palacios et al.^{9,16} of the SU2 team. In the next section we direct the attention of the readers to a new coupled CFD-CAA far-field noise prediction framework developed for the current work.

II.B. Coupled CFD-CAA Noise Prediction using a Permeable Surface Ffowcs Williams-Hawkings Approach

It is known for turbulent flows at low Mach numbers, direct computations of far-field noise is computationally prohibitive.¹⁷ A common way to perform far-field noise prediction is then to adopt a hybrid CFD-CAA approach in which the near-field noise source region is computed using a high-fidelity CFD model and then propagated to the far-field using a computationally cheaper wave equation like CAA model. To that end, integral methods based on the Kirchhoff or Ffowcs Williams-Hawkings (FW-H) formulations offer a more efficient approach for calculating acoustic pressure at arbitrary observer locations by performing boundary integrals once the appropriate field data is known. In this manner, the radiated noise from a complex system can be calculated given the near-field flow data supplied by a CFD solution. In this work, we develop a coupled CFD-CAA far-field noise prediction framework using a permeable surface Ffowcs Williams-Hawkings approach.

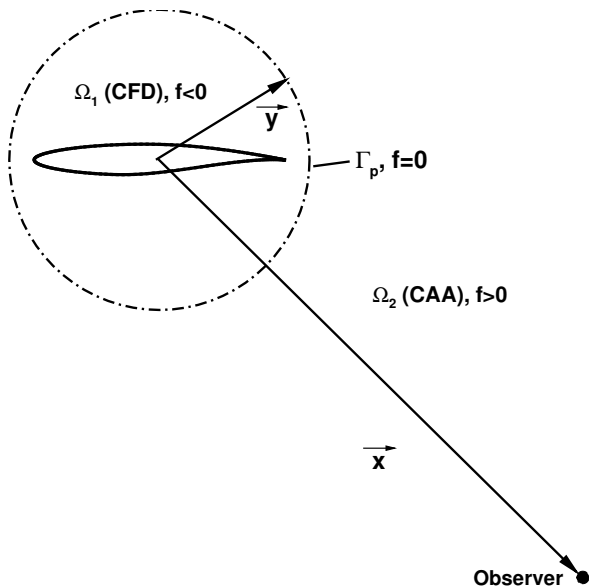


Figure 1. Permeable control surface Γ_p separating the CFD and CAA domains

The permeable FW-H formulation distinguishes itself from its original formulation in that it allows fluid to flow through the discontinuity surface. Consequently, one can define any arbitrary smooth surrounding surface Γ_p around the aerodynamic body S where details of the flow field are extracted and the noise source can be propagated to the far-field. A schematic of such permeable surface is shown on Figure 1. The fluid domain is therefore divided into two regions – the near-field CFD region Ω_1 and far-field CAA region Ω_2 . Further, we define the shape of Γ_p by a function, $f = 0$, such that $f < 0$ inside the control surface and $f > 0$ outside the control surface.

A key difference between this work and an earlier work by Economou et al.⁸ is that in that work the permeable FW-H formulation in the wave equation form is solved directly in time using a finite element method (FEM). In this work we follow the frequency domain formulation presented by Lockard.¹⁹

The permeable surface FW-H equation in the laboratory frame with a fixed source can be written in time domain as:

$$\left(\frac{\partial^2}{\partial t^2} + U_i U_j \frac{\partial^2}{\partial y_i \partial y_j} + 2U_i \frac{\partial^2}{\partial y_i \partial t} - c_\infty^2 \frac{\partial^2}{\partial y_i \partial y_i} \right) [\rho' H(f)] = \frac{\partial}{\partial t} [Q\delta(f)] - \frac{\partial}{\partial y_i} [F_i \delta(f)] + \frac{\partial^2}{\partial y_i \partial y_j} [T_{ij} H(f)] \quad (1)$$

with

$$Q(\vec{y}, t) = [\rho (u'_i + U_i) - \rho_\infty U_i] \hat{n}_i, \quad (2)$$

$$F_i(\vec{y}, t) = [\rho (u'_i - U_i) (u'_j + U_j) + \rho_\infty U_i U_j + p \delta_{ij} - \tau_{ij}] \hat{n}_i, \quad (3)$$

$$T_{ij}(\vec{y}, t) = \rho u'_i u'_j + [p - c_\infty^2 (\rho - \rho_\infty)] \delta_{ij} - \tau_{ij}. \quad (4)$$

where $Q(\vec{y}, t)$, $F_i(\vec{y}, t)$, and $T_{ij}(\vec{y}, t)$ respectively are monopole, dipole and quadrupole source terms on the permeable surface on which $f(\vec{y}) = 0$. The fluctuating flow quantities relative to the free-stream conditions are expressed as: $\rho' = \rho - \rho_\infty$, $u'_i = u_i - U_i$, and $p' = p - p_\infty$. $\delta(f)$ is the Dirac delta function. $H(f)$ is the Heaviside function which is unity for $f > 0$ and zero for $f < 0$. \hat{n}_i denotes the surface normal on Γ_p pointing into the fluid. For three dimensional flows, an efficient time-domain method based on a boundary integral formulation has been developed by Di Francescantonio.²⁰ In two dimensions, a semi-infinite integral appears from the convolution with the appropriate Green function when solving the above FW-H equation in time domain, giving rise to the ‘tail effect’ which requires an infinitely long time to account for all of the source contributions. To circumvent this problem, Equation 1 can be transformed into the frequency domain as follows:

$$\begin{aligned} \left(k^2 - M_i M_j \frac{\partial^2}{\partial y_i \partial y_j} - 2iM_i k \frac{\partial}{\partial y_i} + \frac{\partial^2}{\partial y_i^2} \right) [\tilde{p}'(\vec{y}, \omega) H(f)] = -i\omega [\tilde{Q}(\vec{y}, \omega) \delta(f)] \\ - \frac{\partial}{\partial y_i} [\tilde{F}_i(\vec{y}, \omega) \delta(f)] \\ - \frac{\partial^2}{\partial y_i \partial y_j} [\tilde{T}_{ij}(\vec{y}, \omega) H(f)] \end{aligned} \quad (5)$$

where the quantities denoted by (\sim) have been transformed into the frequency domain and $k = \omega/c_\infty$ is the wavenumber. The free-stream Mach number M_i is defined by $M_i = U_i/c_\infty$. For $M < 1$, the two-dimensional Green function for Equation 5 is obtained from a Prandtl-Glauert transformation and expressed as:

$$G(\vec{x}, \vec{y}, \omega) = \frac{i}{4\beta} \exp\left(\frac{iMk\xi}{\beta^2}\right) H_0^{(2)}\left(\frac{k}{\beta^2} \sqrt{\xi^2 + \beta^2 \eta^2}\right) \quad (6)$$

where

$$\xi = (x_1 - y_1) \cos \theta + (x_2 - y_2) \sin \theta, \quad (7)$$

$$\eta = -(x_1 - y_1) \sin \theta + (x_2 - y_2) \cos \theta \quad (8)$$

$$(9)$$

The incidence angle is defined as $\tan \theta = U_2/U_1$, $H_0^{(2)}$ is the Hankel function of the second kind of order zero, and $\beta = \sqrt{1 - M^2}$ is the Prandtl-Glauert factor. Convolving Equation 5 with the Green function, the pressure fluctuation in frequency domain can be written as:

$$\tilde{p}'(\vec{x}, \omega) = - \oint_{f=0} i\omega \tilde{Q}(\vec{y}, \omega) G(\vec{x}, \vec{y}, \omega) dl - \oint_{f=0} \tilde{F}_i(\vec{y}, \omega) \frac{\partial G(\vec{x}, \vec{y}, \omega)}{\partial y_i} dl - \int_{f>0} \tilde{T}_{ij}(\vec{y}, \omega) \frac{\partial^2 G(\vec{x}, \vec{y}, \omega)}{\partial y_i \partial y_j} dl \quad (10)$$

For the types of low speed flows examined in this work, the contribution of quadrupole sources is typically negligible in comparison to the monopole and dipole terms. In addition, the inclusion of the quadrupole term would entail the computationally expensive evaluation of a surface integral over the entire domain outside of the permeable surface. Therefore, the quadrupole term is neglected in the evaluation of Equation 10. The CAA module is implemented and interfaced with the remainder of the SU2 suite as follows: an unsteady flow simulation is first performed. At every time step, the primitive flow variables at each point on the permeable surface are extracted and the monopole and dipole source terms computed using Equations 2 and 3. At the end of the CFD simulation, the respective mean values are

subtracted from Q and F_i as they correspond to zero frequency components which do not generate any noise. Due to the fact that it is practically impossible to ensure perfectly periodic flow data from most CFD calculations, a Hanning-type windowing function is applied to the zero-mean source terms Q and F_i to prevent spectral leakage.^{5,19} The windowed source terms are then Fourier transformed using fast Fourier transformation (FFT). The pressure fluctuation in frequency domain can be computed by numerically integrating along the permeable surface, for each observer location $\bar{\mathbf{x}}$ and frequency ω . Finally, pressure fluctuation $p'(\bar{\mathbf{x}}, t)$ in time domain can be recovered using an inverse FFT.

II.C. AD-based Unsteady Discrete Adjoint Framework

The implementation of the discrete adjoint formulation in this work is eased by the use of automatic differentiation (AD)^a, eliminating the error-prone hand-differentiation of the discretized equations. AD was developed based on the observation that any simulation code, regardless of its complexity is merely a sequence of elementary operations whose differentiation rules are well known. Therefore, by successive applications of the chain-rule through the computer program, it is possible to compute both the simulation output and its derivative with respect to prescribed design variables simultaneously. A remarkable feature of AD, owing to its construction, is that it does not incur any truncation errors compared to the traditional finite difference method. In particular, the derivatives are accurate to machine accuracy. This is a very attractive characteristic of AD, since accurate evaluation of the gradient requires exact differentiation of the fixed point iterator G^n as evidenced by Equations 24 and 25 in the following discussion.

The AD can be performed in the forward and reverse (adjoint) mode. The forward mode, albeit exact, requires one evaluation for each component of the gradient vector. In contrast, the reverse mode is capable of computing the entire gradient vector in one stroke of the forward and reverse simulation in time. For this reason, the reverse mode is also referred to as the adjoint mode. The one-stroke gradient computation of the reverse mode AD is achieved at the expense of high memory requirement due to the need to save all intermediate variables in an unsteady computation. For this reason, wherever the adjoint mode is used in this study, it is always implemented in conjunction with the memory-saving checkpointing technique, which stores the flow solution at certain points in time during the forward sweep as *checkpoints*. The flow solutions are then recomputed from these checkpoints in the reverse sweep for adjoint variables. The maximum number of time steps allowable between the two consecutive checkpoints is dictated by the memory available at each core. For long time computations, the many checkpoints required results in high hard disk storage requirement and an increase in run time due to the need to recompute the flow solutions as well as reading and writing of large volumes of data at each checkpoint. A good discussion of the two AD modes along with checkpointing techniques can be found in.^{22,23}

Now we present our AD-based unsteady discrete adjoint framework using a simple system of PDEs as an example. For the sake of brevity, influences of the mesh are omitted. Consider a system of semi-discretized PDEs as follows:

$$\frac{dU}{dt} + R(U) = 0 \quad (11)$$

where U is the spatially discretized state vector and $R(U)$ is the discrete spatial residual vector. For the sake of illustration, we assume the second-order backward difference is used for time discretization, which leads to the following system of equations:

$$R^*(U^n) = \frac{3}{2\Delta t}U^n + R(U^n) - \frac{2}{\Delta t}U^{n-1} + \frac{1}{2\Delta t}U^{n-2} = 0, \quad n = 1, \dots, N \quad (12)$$

The application of dual-time stepping method then solves the following problem through a fictitious time τ to converge to a steady state solution in (12):

$$\frac{dU^n}{d\tau} + R^*(U^n) = 0 \quad (13)$$

Further assume the implicit Euler method is used to time march the above equation to steady state.

$$U_{p+1}^n - U_p^n + \Delta\tau R^*(U_{p+1}^n) = 0, \quad p = 1, \dots, M \quad (14)$$

The resultant nonlinear system can be linearized around U_p^n to solve for the state U_{p+1}^n

$$U_{p+1}^n - U_p^n + \Delta\tau \left[R^*(U_p^n) + \frac{\partial R^*}{\partial U} \bigg|_p (U_{p+1}^n - U_p^n) \right] = 0, \quad p = 1, \dots, M \quad (15)$$

^aperformed using AD tool ADEPT¹⁰

This can be written in the form of a fixed-point iteration:

$$U_{p+1}^n = G^n(U_p^n, U^{n-1}, U^{n-2}), \quad p = 1, \dots, M, \quad n = 1, \dots, N \quad (16)$$

where G^n represents an iteration of the pseudo time stepping. U^{n-1} and U^{n-2} are the converged state vectors at time iterations $n-1$ and $n-2$ respectively. The fixed point iteration converges to the numerical solution U^n :

$$U^n = G^n(U^n, U^{n-1}, U^{n-2}), \quad n = 1, \dots, N \quad (17)$$

The discrete optimization problem can then be posed as:

$$\min_{\alpha} \quad J = f(U^{N_*}, \dots, U^N, \alpha) \quad (18)$$

$$\text{subject to} \quad U^n = G^n(U^n, U^{n-1}, U^{n-2}, \alpha), \quad n = 1, \dots, N \quad (19)$$

where α is the vector of design variables and the objective function J is evaluated between $N_* \leq n \leq N$. One can express the Lagrangian associated with the above constrained optimization problem as follows:

$$L = f(U^{N_*}, \dots, U^N, \alpha) - \sum_{n=1}^N [(\bar{U}^n)^T (U^n - G^n(U^n, U^{n-1}, U^{n-2}, \alpha))] \quad (20)$$

where \bar{U}^n is the adjoint state vector at time level n . The first order optimality conditions are given by:

$$\frac{\partial L}{\partial \bar{U}^n} = 0, \quad n = 1, \dots, N \quad (\text{State equations}) \quad (21)$$

$$\frac{\partial L}{\partial U^n} = 0, \quad n = 1, \dots, N \quad (\text{Adjoint equations}) \quad (22)$$

$$\frac{\partial L}{\partial \alpha} = 0, \quad (\text{Control equation}) \quad (23)$$

From (22), the unsteady discrete adjoint equations can be derived in the fixed point form as:

$$\bar{U}_{i+1}^n = \left(\frac{\partial G^n}{\partial U^n} \right)^T \bar{U}_i^n + \left(\frac{\partial G^{n+1}}{\partial U^n} \right)^T \bar{U}^{n+1} + \left(\frac{\partial G^{n+2}}{\partial U^n} \right)^T \bar{U}^{n+2} + \left(\frac{\partial f}{\partial U^n} \right)^T, \quad n = N, \dots, 1 \quad (24)$$

where \bar{U}^{n+1} and \bar{U}^{n+2} are converged adjoint state vectors at time levels $n+1$ and $n+2$. The unsteady adjoint equations above are solved backward in time. At each time level n we iterate through inner iteration i until we have converged to \bar{U}^n . The highlighted terms here are evaluated in reverse mode AD at each iteration. To do so, reverse accumulation²² is performed at the beginning of each time level n to store the computational graph by evaluating G using converged state solution U_n . Then each inner iteration i proceeds by re-evaluating the tape using the updated adjoint vector \bar{U}_i^n , giving the highlighted terms. This continues within each time level n until the adjoint vector has converged to \bar{U}^n . Note that $\frac{\partial f}{\partial \bar{U}^n} = 0$ for $n < N_*$. The sensitivity gradient can then be computed from the adjoint solutions:

$$\frac{dL}{d\alpha} = \frac{\partial f}{\partial \alpha} + \sum_{n=1}^N \left((\bar{U}^n)^T \frac{\partial G^n}{\partial \alpha} \right) \quad (25)$$

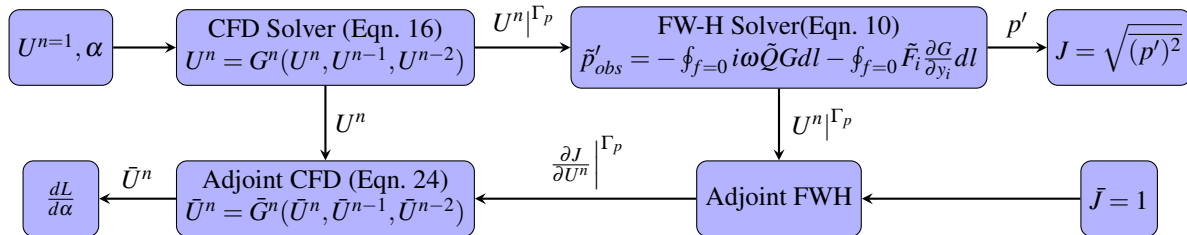


Figure 2. Computational chain of the coupled CFD-FWH noise prediction and optimization framework

The computational chain for the coupled CFD-FWH noise prediction and noise-adjoint framework is outlined on Figure 2. In the primal phase, unsteady flow field U^n is realized at each time step n by the SU2 CFD solver via Equation 16. $U^n|_{\Gamma_p}$ denotes the conservative flow variables at time step n extracted from the FW-H surface Γ_p which are then passed to the FW-H solver for far-field noise computation via Equation 10. In the adjoint phase, $\frac{\partial J}{\partial U^n}|_{\Gamma_p}$ denotes the sensitivity of the noise objective with respect to conservative flow variables evaluated Γ_p by the adjoint FW-H solver using $U^n|_{\Gamma_p}$, which is accumulated to the fixed-point iteration for the adjoint flow variables \bar{U}^n in the adjoint CFD solver (Equation 24).

In this work, we apply the operator overloading AD method with expression template technique¹⁰ to the SU2 suite. This leads to additional flexibilities in the resultant discrete adjoint framework – the adjoint solver can be automatically updated with primal code modification and one can easily define any objective function from any state variable. This is an extremely attractive characteristic for unsteady optimization problems in the multidisciplinary setting using a suite of multi-physics solvers where the objective function may be different depending on the type of problems being addressed.

III. Validation

III.A. Validation of the Hybrid CFD-FWH Solver

To validate the hybrid CFD-FWH noise prediction framework, we first examine the canonical test case of laminar ($Re = 100$) vortex shedding of a circular cylinder in subsonic flow ($M_\infty = 0.2$). The mesh used is an O-mesh with 12,800 nodes. The permeable FW-H surface is a circle of diameter $D_{FWH} = 3.0$ concentric to the cylinder which has a diameter $D = 1.0$. The CFD solution is computed using the second-order dual time-stepping method with a time step of $\Delta t = 0.001$. The flow around the cylinder is allowed to evolve and settle into a periodic steady state before 1024 samples are recorded at each of the 128 source points on the FW-H surface.

The pressure fluctuations computed using the hybrid approach is compared with the static pressure fluctuations directly extracted from the CFD data at three observer locations situated at $3D$, $5D$ and $10D$ below the cylinder as show on Figure 3. The Hanning window (scaled to the same magnitude as the fluctuation for the sake of visualization) used to enforce the periodicity of the flow data is also plotted. It can be seen that in the middle 3/4 of the signal, the agreement in both amplitude and frequency between the CFD-only and the hybrid CFD-FWH solutions is excellent at all three observer locations. The slight over-prediction of amplitude is due to the fact that the Hanning window is designed to be energy preserving but not necessarily amplitude preserving. Figure 4 shows a comparison between the root-mean-square of the pressure fluctuation computed using both approaches over a circle at a radius of $10D$ around the cylinder. Good agreement is obtained almost omni-directionally between the two methods except for a small region upstream where the acoustic cancellation effect related to the refraction of waves propagating upstream is not captured by the FW-H solver due to the lack of the quadrupole source term. However, in most of the directions below the cylinder, where the accuracy of the aeroacoustic prediction is of the most practical importance, the agreement is excellent.

Next, the hybrid solver is validated for the turbulent case ($Re = 1.2 \times 10^6$) with the cylinder at the same Mach number. The turbulence is modeled by the Spalart-Allmaras model. The O-mesh used in this case has 96,000 nodes. The pressure fluctuations computed using the direct and hybrid approaches are compared at three observer locations situated at $5D$, $10D$ and $15D$ below the cylinder as show on Figure 5. As in the laminar case, the agreement is excellent.

III.B. Validation of Coupled CFD-CAA Adjoint

The SU2 suite has been differentiated using AD in both forward and reverse (adjoint) modes. Furthermore, check-pointing and reverse accumulation have also been implemented for the adjoint mode at each time iteration. For noise-minimization cases, the objective function is defined as the root-mean-square of the acoustic pressure averaged over N_{obs} observer locations. The noise-specific coupled sensitivities are computed as outlined in Section II.C.

The coupled aeroacoustic sensitivities are validated for both laminar and turbulent flows via the same cylinder vortex shedding test cases used to validate the CFD-FWH solver in the previous subsection. The surface sensitivities at 18 different circumferential positions on the cylinder surface are computed using both second order central difference and AD-based adjoint over 10 time steps. The comparisons are shown on Figure 6 (a) for the laminar case and Figure 6 (b) for the turbulent case. It is clear that AD-based adjoint attains very good accuracy. It must also be noted that as the integration time increases, the accuracy of finite difference will deteriorate, often to the order of the sensitivity itself, while AD-based adjoint incurs no round-off error and maintains high accuracy over long integration

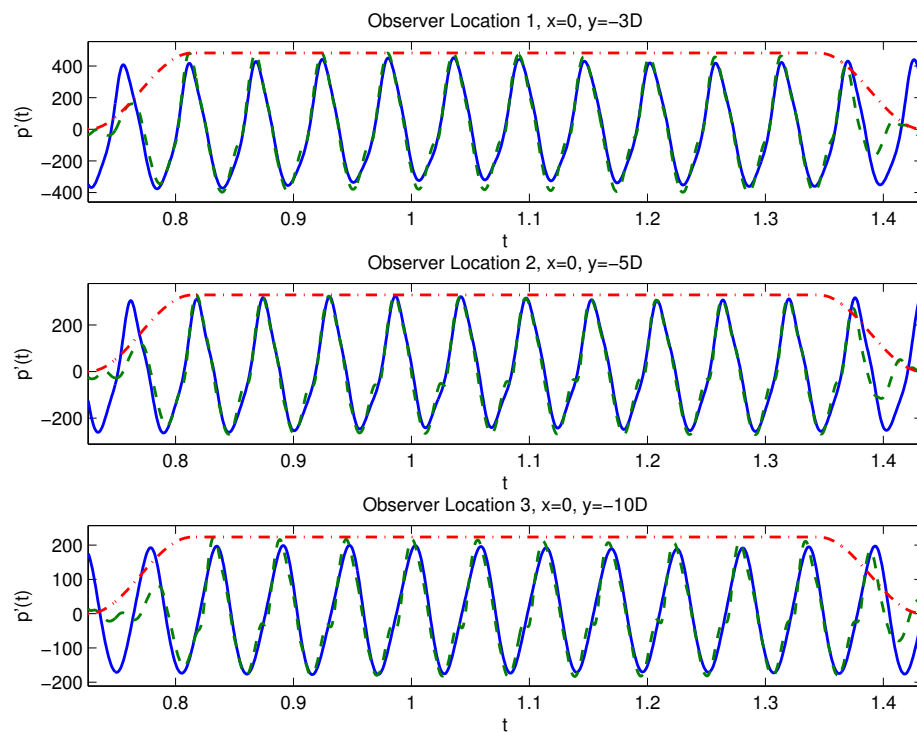


Figure 3. Comparison of acoustic signals at three observer locations in the laminar vortex shedding case (—: CFD-only; ---: CFD-FWH; -.-: Hanning Window)

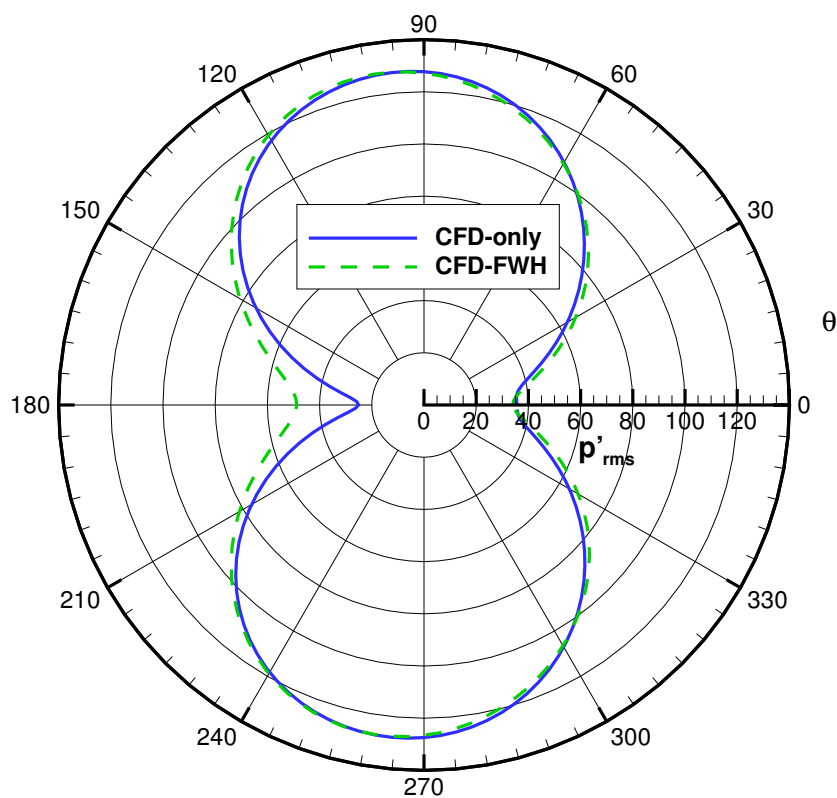


Figure 4. Directivity comparison at $R_{obs} = 10D$ for the laminar vortex shedding case

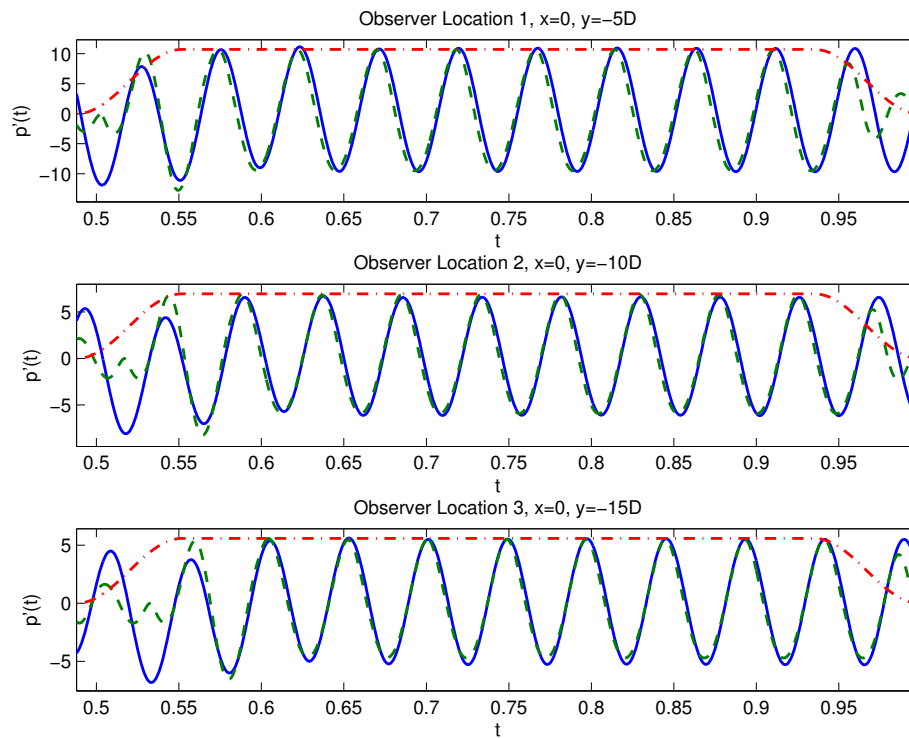


Figure 5. Comparison of acoustic signals at three observer locations in the turbulent vortex shedding case (—: CFD-only; ---: CFD-FWH; -.-: Hanning Window)

times.

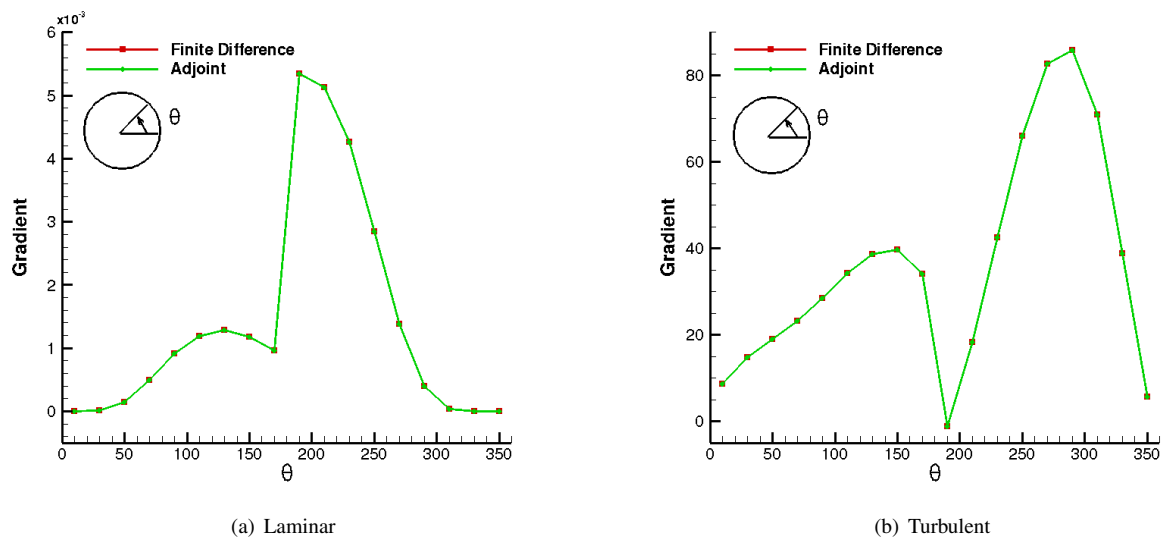


Figure 6. Comparison between the gradients computed using finite difference (second order central difference with a step size of 10^{-6}) and adjoint mode of AD, at various angular positions around the cylinder surface.

IV. Optimization Results

In the subsequent subsections, we present optimization results from aerodynamic and aeroacoustic optimization problems involving dynamic mesh movement routine and various turbulence model, as well as the hybrid CFD-CAA design chain – all of which can be cumbersome and error-prone tasks using the continuous adjoint and hand-discrete approaches.

IV.A. Lift-Constrained Drag Minimization of a Pitching Airfoil in Transonic Turbulent Flow

In this test case, we consider the lift-constrained drag minimization problem of an RAE2822 airfoil in transonic ($M_\infty = 0.8$) and turbulent ($Re = 6.5 \times 10^6$) flow regime, pitching about its quarter-chord point with a mean angle of attack of 2.0 degrees, an amplitude of 3.0 degrees and a frequency of 251.3 rad/s.

The mesh used is an un-structured, O-grid that wraps around the RAE 2822 airfoil. It has 22,842 elements in total with 192 edges making up the airfoil boundary and 40 edges along the far field boundary. It is a hybrid-element mesh with quadrilaterals in the region adjacent to the airfoil surface and triangles in the remaining portion of the computational domain. The first grid point of the airfoil surface is at a distance of 10^{-5} chord, and the far field boundary is located approximately one hundred chord lengths away from the airfoil. Characteristic-based far-field boundary conditions are enforced on the far-field boundary, and a no-slip, adiabatic boundary condition is enforced on the airfoil. The convective fluxes are computed using the Jameson-Schmidt-Turkel (JST) scheme while the turbulent viscosity is calculated using the Menter Shear Stress Transport (SST) Model. A time step of 0.001 is used for the dual time-stepping, resulting in 25 time steps per period of oscillation for a total of 8 periods.

A total of 38 Hicks-Henne bump functions are chosen as design variables and they are equally spaced along the upper and lower surfaces of the airfoil (19 on each of the upper and lower surfaces). The objective function is defined as the time-averaged drag within the periodic steady state:

$$J_D = \bar{C}_d = \frac{1}{N - N_*} \sum_{n=N_*+1}^N C_d^n \quad (26)$$

where C_d^n is the instantaneous drag coefficient at time level n . N is the total number of time steps and N_* is the number of time steps before entering the optimization window in which \bar{C}_d is to be minimized as shown on Figure 10. In this case $N_* = 50$ and the optimization window contains 6 periods of oscillation. The time-average lift \bar{C}_l is constrained in the optimization so that $\bar{C}_l^{Optimized} = \bar{C}_l^{RAE2822} = 0.4$. A volume constraint is also imposed to ensure that the volume of the optimized airfoil remains at least as large as the baseline RAE2822 airfoil.

The time-averaged drag is reduced by 38% after 24 CFD evaluations, while the mean lift is maintained at $\bar{C}_l = 0.4$, as shown on Figure 7 (a). A comparison between the baseline RAE2822 and the new airfoil profiles is shown on Figure 7 (b). Note that the curvature in the first 50% chord has been drastically reduced in the optimized airfoil, since the airfoil is pitching at a positive mean angle of attack. The effect can be seen by comparing the Mach number contour of the airfoils at their mean (Figure 8 (b) and Figure 9 (b)) and maximum (Figure 8 (c) and Figure 9 (c)) angles of attack – the shock strength on the upper surface has been significantly reduced, although the presence of the mean lift and volume constraints prevents the shock from being fully removed. Note that at all three angles shown on Figure 8 and Figure 9, the shock position has moved further downstream in the ‘improved airfoil’, reducing the extent of shock-induced separation on the airfoil surface. Consequently, the new airfoil achieves lower drag within the optimization window as shown on Figure 10. The time-averaged drag is reduced by 38% from the baseline value.

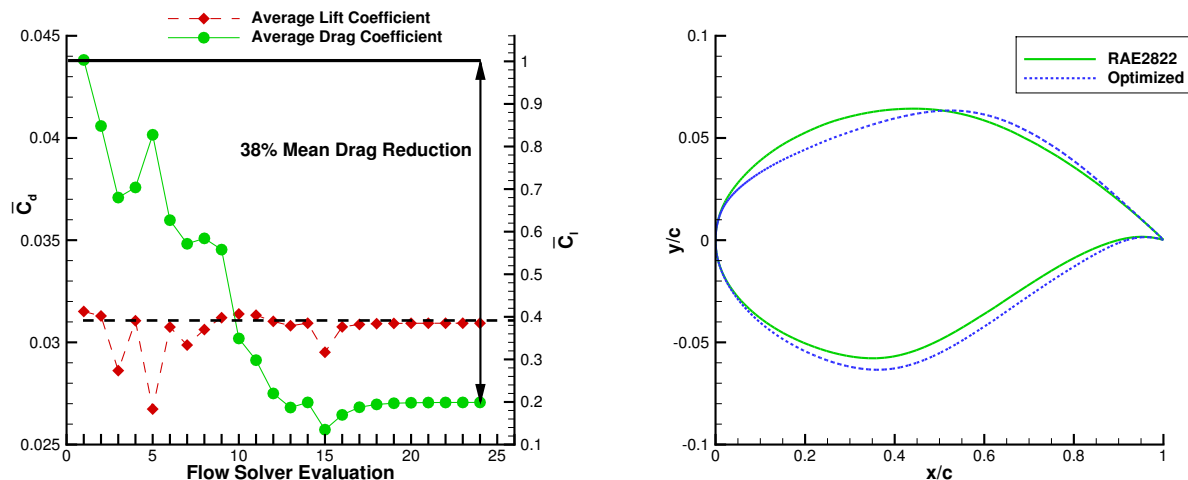
IV.B. Drag and Noise Minimization of a Circular Cylinder Undergoing Periodic Vortex Shedding

In this test case, we apply the AD-based discrete adjoint framework to the drag and noise minimization problem of a circular cylinder undergoing periodic vortex shedding. The computational mesh as well as the flow conditions remain the same as the validation case presented in Section III.A, except for the angle of attack which is increase to 10 degrees.

In both drag and noise minimization cases presented here, the unsteady simulations are performed using a second-order accurate dual time-stepping scheme with 30 time steps per shedding period.

A total of 38 Hicks-Henne bump functions are chosen as design variables and they are equally spaced along the upper and lower surfaces of the cylinder (19 on each of the upper and lower surfaces).

For the drag minimization problem, the objective function is defined by Equation 26. For the noise-minimization problem, the objective function is defined as the time-averaged pressure fluctuation within the periodic steady state at



(a) Optimization convergence history of time-averaged drag and lift coefficients.

(b) Comparison between the baseline RAE2822 airfoil and the optimized airfoil

Figure 7. Optimization convergence history and the comparison between the baseline RAE2822 airfoil and the optimized airfoil

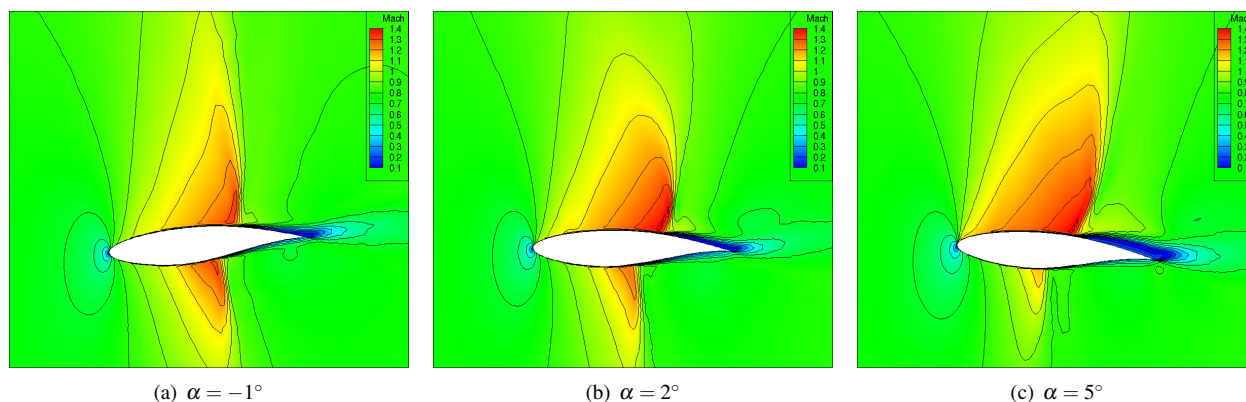


Figure 8. Mach number contour of the baseline RAE2822 airfoil at various time instances over one period

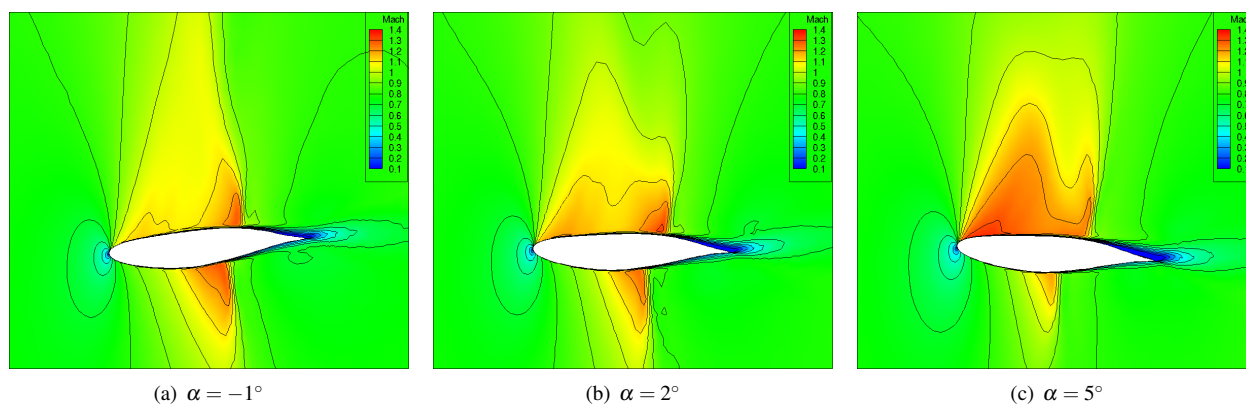


Figure 9. Mach number contour of the optimized airfoil at various time instances over one period

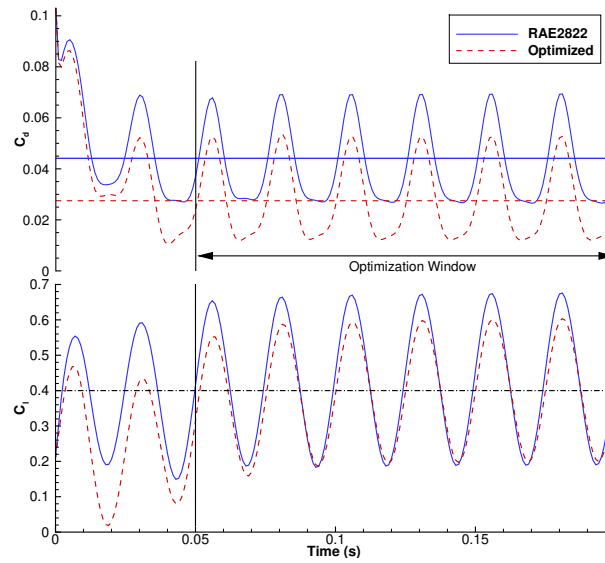


Figure 10. Time history of lift and drag coefficients of the RAE2822 and the optimized airfoil. The horizontal lines denote time-averaged values

an observer location:

$$J_N = \frac{1}{N_{obs}} \sum_{m=1}^{N_{obs}} \sqrt{\frac{1}{N - N_*} \sum_{n=N_*+1}^N (p'_{n,m})^2} \quad (27)$$

where $p'_{n,m}$ is the pressure fluctuation at time level n and observer location m computed using the frequency domain FW-H solver introduced in Section II.B. Three observation locations are placed equidistantly along a line $20D$ below the cylinder at $(-20D, -20D)$, $(0, -20D)$, and $(20D, 20D)$. N is the total number of time steps and N_* is the number of time steps before entering the optimization window in which the magnitude of the pressure fluctuation is to be minimized. In this case $N_* = 512$ and the optimization window contains 6 periods of pressure fluctuation measured at the three observation points.

For both drag and noise minimization cases, the thickness constraints are imposed at $x = 1/4, 1/2$ and $3/4$ such that the thickness at these locations must be at least $0.15D$.

A drag minimization is first performed on the baseline cylinder. The time-averaged drag is reduced by 96.1% after 18 design updates, as shown on Figure 11 (a). A comparison of the time histories of C_d between the baseline and the optimized geometry is shown on Figure 11 (b). Not only is the time-averaged drag significantly reduced, but also is the amplitude of oscillation, indicating that the periodic vortex shedding has been eliminated.

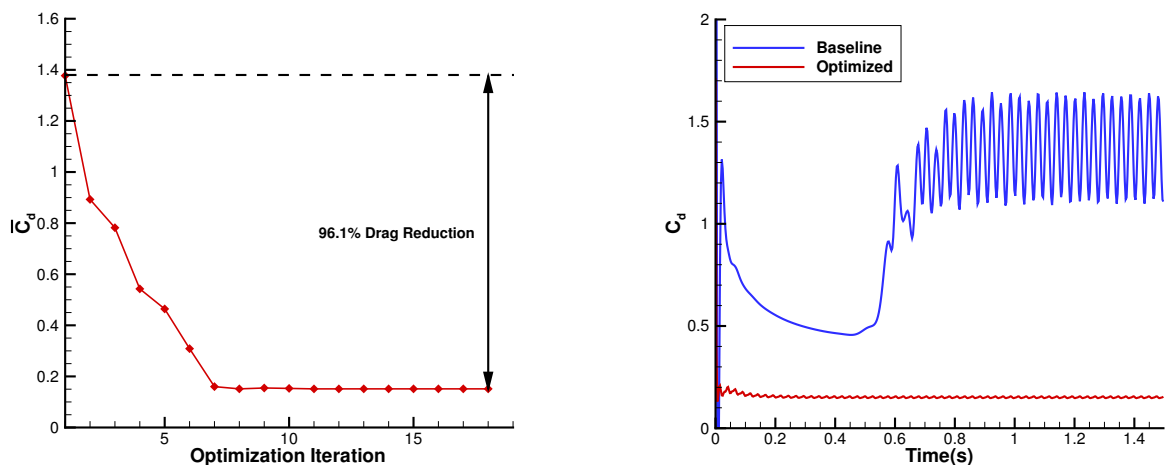
Next, a noise minimization is performed on the baseline cylinder. The root-mean-square of the pressure fluctuation at the three observer locations is reduced by 47.8% after 12 CFD evaluations, as shown on Figure 12. A comparison of the time histories of $p'(t)$ between the baseline and the optimized geometry at the three observer locations is shown on Figure 13. It can be seen that the magnitude of pressure fluctuation is significantly reduced over the optimization window for the optimized design. Furthermore, the directivity plot on Figure 14 demonstrates that the drastic noise reduction achieved by the optimized design is omni-directional.

Figure 15 compares the two optimal geometries with the baseline cylinder. The drag-minimized geometry has its profile significantly reduced to prevent the rise of pressure drag due to periodic vortex shedding. In fact, the optimizer is not able to further thin the profile due to the thickness constraint that is active at the quarter-chord location. Since the flow is impinging on the body at an 10 degree angle, the chord-line of the optimized geometry is also tilted downward to streamline itself towards the incoming flow, preventing leading-edge separation. It is interesting to note that the noise-minimized geometry in comparison is much thicker. Evidently in this case, the reduction of far-field noise level does not necessitate an aggressive thinning of the profile. This serves to illustrate the fact that an aerodynamically superior design may not necessarily be favorable in its aeroacoustic performance and vice versa.

Comparing the performance of the two optimal designs in terms of both drag and noise objectives on Table 1, it can be seen that when the drag-minimized design is analyzed for noise, it results in a significantly lower noise level. This is not surprising since the noise in the cylinder shedding case is dominated by the lift dipole and the thinning

of the profile in the drag-minimized design reduces the magnitude of lift oscillation. In a similar study conducted by Rumpfkeil and Zingg,⁵ the reverse trend is noted – the drag-minimized airfoil results in a noise objective value that is twice as high as the noise-minimized one. While their study was performed for a blunt trailing edge in the turbulent flow regime, it is apparent from their work and this test case that whether the drag and noise are two competing design objectives can be highly case-dependent. The fact that the optimizer converged to a different design in the noise-minimized case also shows that aeroacoustic optimization problems may be challenged by the existence of multiple local minima.

It is clear from the study of this simple test case that drag and noise minimizations do not lead to the same optimal shape. Moreover, if conducted in parallel, they may not even result in the similar optimal performance in this two-objective problem in that a noise-minimized design may lead to unsatisfactory rise in drag. This serves to illustrate an important point that aeroacoustic optimization cannot be an ‘after-thought’ – it must be included in the initial design process in order to minimize its impact on other aerodynamic performances. While design and optimization using steady aerodynamics for lift and drag is still the industry standard today, to reduce aerodynamic noise – an inherently unsteady phenomenon, efficient unsteady simulation and design tools are of paramount importance. To that end, the AD-based discrete adjoint framework developed on the basis of the SU2 multi-physics software suite offers an accurate and robust way to tackle challenges arising from the unsteady aeronautical design problems.



(a) Optimization convergence history of time-averaged drag coefficient.

(b) Time history of C_d for the baseline cylinder and the optimized geometry

Figure 11. Drag minimization result of a circular cylinder in laminar subsonic flow

	Cylinder	Drag Minimized	Noise Minimized
J_D	1.353	0.0521	0.8883
J_N	59.584	13.703	31.122

Table 1. Comparison between drag minimization and noise minimization results

IV.C. Lift Maximization and Noise Minimization of a Wing-Flap Geometry

In this subsection, we apply the coupled CFD-FWH optimization framework to a more realistic test case – the NLR7301 wing-flap geometry in landing configuration at an angle of attack of 15 degrees, with the flap deflected at 30 degrees (Figure 16). The freestream Mach number is $M_\infty = 0.2$. Laminar flow is assumed with $Re = 800$.

As shown on Figure 16, the first 15% chord of the main wing nose region is parameterized by the free form deformation (FFD) box with 64 control points and allowed to be morphed by the optimizer. The remainder of the main wing, as well as the flap remain fixed throughout the optimization. An unstructured O-mesh is used for this geometry with 39,000 triangular elements.

Both lift maximization and noise minimization are performed. The optimizations are performed over 1200 time steps at $\Delta t = 0.001$. The optimization window is defined to be the last 512 time steps which approximately correspond

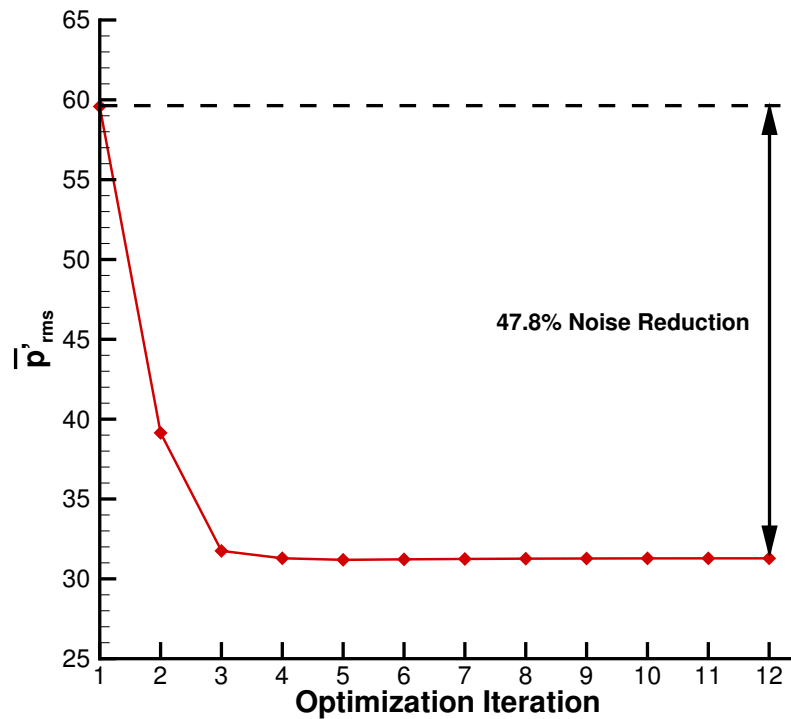


Figure 12. Optimization convergence history of the root-mean-square of pressure fluctuation, averaged over three observer locations

to 4 periods of vortex shedding. The corresponding convergence histories for the two optimization cases are shown on Figure 17 (a) and (b). For the noise minimization case, the observer locations are the same as the previous cylinder shedding case. Note that since the shape change is only restricted to the first 15% chord of the main wing, the improvements in the lift and noise performances are not as drastic as the cylinder case. However, it is clear that the time averaged lift is significantly improved while the acoustic pressure is decreased.

Figure 18 shows a comparison between the two optimized geometries with the baseline NLR7301 geometry. It can be seen that to maximize lift, the optimizer morphs the nose downward. Consequently the optimized geometry bears a striking resemblance to the droop-nose designs that can be found on a number of aircraft currently in service. The noise-minimized design, however, tilts the nose the other way – in the upwards direction. The two entirely different optimal designs obtained here serve to further underline the point that aerodynamically and aeroacoustically optimized designs can be drastically different. The fact that the aerodynamic and aeroacoustic design objectives are mutually competing is illustrated by the performance comparison on Table 2 where the lift maximized design is analyzed for its noise level and the noise minimized design for its lift performance. The red off-diagonal entries clearly show that the noise minimized design is accompanied by a marked loss of lift even from the baseline design while the lift maximized design led to an amplification of noise level.

	NLR7301	Lift Maximized	Noise Minimized
J_L	1.9001	1.9980	1.8692
J_N	2.1407×10^{-3}	2.5369×10^{-3}	2.0556×10^{-3}

Table 2. Performance comparison between lift maximization and noise minimization results

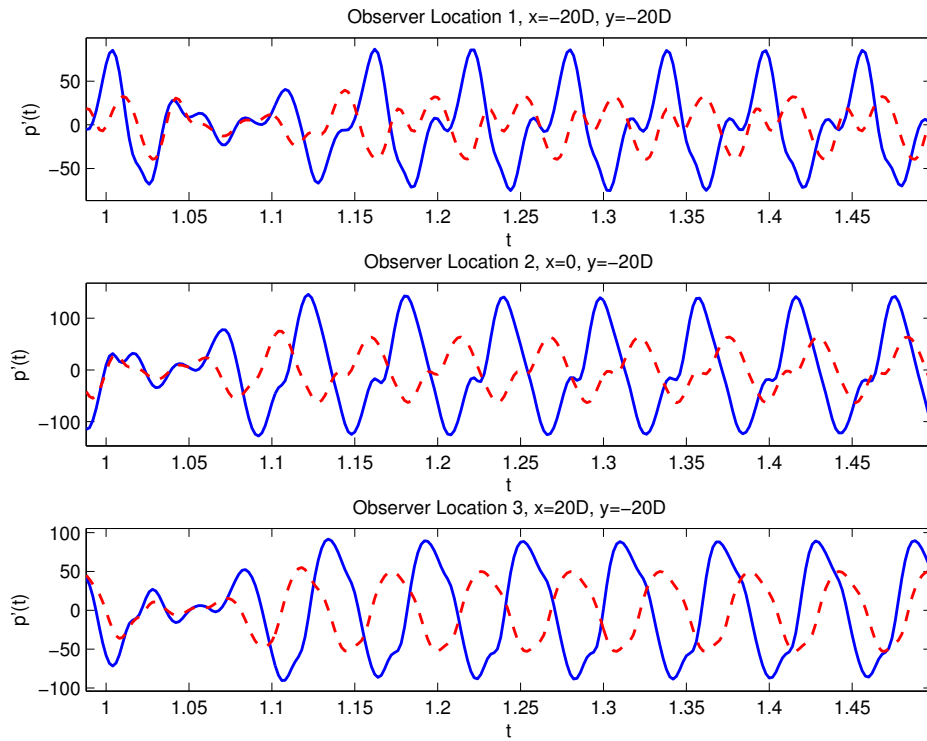


Figure 13. Comparison of the pressure fluctuation at three observer locations between the baseline (—) and optimized (---) designs, within the optimization window

V. Conclusion

In this paper, we present an unsteady aerodynamic and aeroacoustic optimization framework in which algorithmic differentiation (AD) is applied to the open-source multi-physics solver SU2 to obtain design sensitivities. An AD-based consistent discrete adjoint solver is developed which directly inherits the convergence properties of the primal flow solver due to the differentiation of the entire nonlinear fixed-point iterator. This includes the differentiation of the dynamic mesh movement routine and various turbulence model, as well as the hybrid CFD-CAA design chain – all of which can be cumbersome and error-prone using the continuous adjoint and hand-discrete approaches.

The results demonstrate that the unsteady adjoint information provided by this AD-based discrete adjoint framework is accurate and robust. The aerodynamic and noise objective values are significantly improved in both cases. The second and third case studies show that aerodynamic and noise minimizations do not yield the same optimal shape and the noise minimization problems may be faced with multiple local minima. Furthermore, it is possible for a noise-minimized design to result in an unacceptable deterioration in the aerodynamic performance. This highlights the need for efficient simulation and design tools tailored for unsteady problems in order to take both aerodynamic and acoustic performances into account in the early stage of the design process.

VI. Acknowledgement

The first author would like to acknowledge the partial funding by the Natural Science and Engineering Research Council of Canada (NSERC). The authors would also like to gratefully acknowledge Dr. Markus Hillenbrand of the RHRK high performance computing center for his support in procuring essential computational resources via the ‘Elwetritsch’ high performance cluster at the TU Kaiserslautern.

References

- ¹Pironneau, O. On optimum design in fluid mechanics. *Journal of Fluid Mechanics* **64**, 97–110 (1974).
- ²Jameson, A. Aerodynamic design via control theory. *Journal of Scientific Computing* **3**, 233–260 (1988).

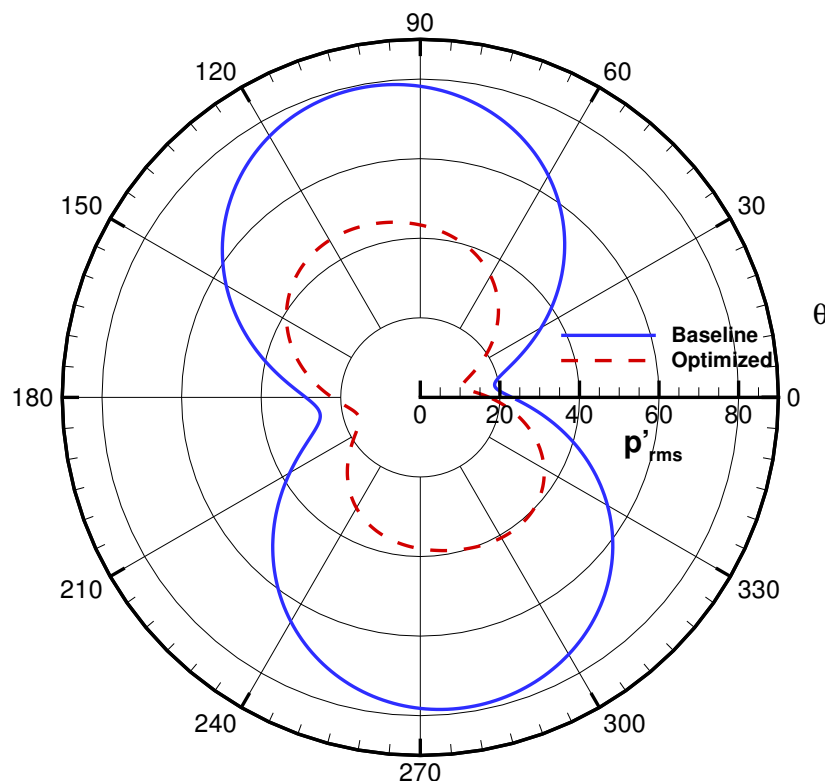


Figure 14. Comparison of directivity between the baseline and optimized designs

³Kenway, G. K. W. and Martins, J. R. R. A. Multipoint high-fidelity aerostructural optimization of a transport aircraft configuration. *Journal of Aircraft* **51** (1), 144–160 (2014).

⁴Lyu, Z. and Martins, J. R. R. A. Aerodynamic design optimization studies of a blended-wing-body aircraft. *Journal of Aircraft* **51** (5), 1604–1617 (2014).

⁵Rumpfkeil, M. P. and Zingg, D. W. A hybrid algorithm for far-field noise minimization. *Computers and Fluids* **39**(9), 1516–1528 (2010).

⁶Mani, K. and Mavriplis, D. J. Unsteady discrete adjoint formulation for two-dimensional flow problems with deforming meshes. *AIAA Journal* **46**(6), 1351–1364 (2008).

⁷Nielsen, E. J. and Diskin, B. Discret adjoint-based design for unsteady turbulent flows on dynamic overset unstructured grids. *AIAA Paper*, 2012-0554 (2012).

⁸Economou, T. D., Palacios, F., and Alonso, J. J., A coupled-adjoint method for aerodynamic and aeroacoustic optimization. *AIAA Paper* 2012-5598, (2012).

⁹Economou, T. D., Palacios, F., and Alonso, J. J., An unsteady continuous adjoint approach for aerodynamic design on dynamic meshes. *AIAA Paper* 2014-2300, (2014).

¹⁰Hogan, R. Fast reverse-mode automatic differentiation using expression templates in C++. *Transactions on Mathematical Software* **40** (26), 1–16 (2014).

¹¹Hovland, P., Mohammadi, B., and Bischof, C., Automatic differentiation and Navier-Stokes computations. *Computation Methods for Optimal Design and Control*, 265–284 (1998).

¹²Gauger, N. R., Walther, A., Moldenhauer, C., and Widhalm, M., Automatic differentiation of an entire design chain for aerodynamic shape optimization. *Notes on Numerical Fluid Mechanics and Multidisciplinary Design* **96**, 454–461 (2007).

¹³Nemili, A., Özkaya, E., Gauger, N., Kramer, F., Höll, T., and Thiele, F., Optimal design of active flow control for a complex high-lift configuration. *AIAA Paper* 2014-2515, (2014)

¹⁴Lockard D. P. and Lilley G. M. The Airframe Noise Reduction Challenge. *NASA Report*, (2004).

¹⁵Colonius, T. and Lele, S. K. Computational Aeroacoustics: Progress on Nonlinear Problems of Sound Generation. *Progress in Aerospace Sciences* **40**, 345–416 (2004).

¹⁶Palacios, F., Economou, T. D., Aranake, A. C., Copeland, S. R., Lonkar, A. K., Lukaczyk, T. W., Manosalvas, D. E., Naik, K. R., Padron, A. S., Tracey, B., Variyar, A., and Alonso, J. J., Stanford University Unstructured (SU2): Open-source analysis and design technology for turbulent flows. *AIAA Paper* 2014-0243, (2014)

¹⁷Colonius, T., and Lele, S. K., Computational aeroacoustics: progress on nonlinear problems of sound generation. *Progress in Aerospace Sciences* **40**, 345–416 (2004).

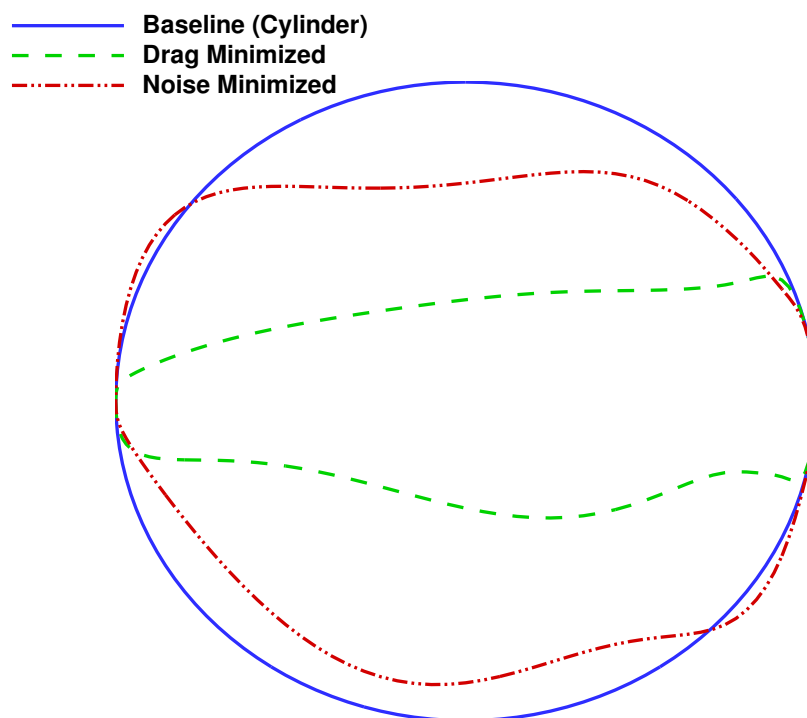


Figure 15. Comparison between the baseline (cylinder), drag minimized and noise minimized designs

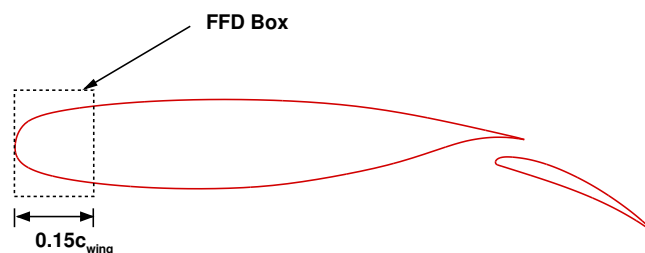


Figure 16. The NLR7301 wing-flap geometry. The dashed box shows the nose region controlled by free form deformation

¹⁸Herr, M., Rossignol, K., Delfs, J., Möner, M., and Lippitz, N., Specification of porous materials for low-noise trailing-edge applications. *AIAA Paper 2014-3041*, (2014)

¹⁹Lockard, D. P., An Efficient, Two-Dimensional Implementation of the Ffowcs Williams and Hawkins Equation. *Journal of Sound and Vibration* **229**(4), 897–911 (2000).

²⁰Di Francescantonio, P., A New Boundary Integral Formulation for the Prediction of Sound Radiation. *Journal of Sound and Vibration* **202**(4), 491–509 (1997).

²¹Lyrantzis, A. S., Surface integral methods in computational aeroacoustics – From the (CFD) near-field to the (Acoustic) far-field. *International Journal of Aeroacoustics* **2**(2), 95–128 (2003).

²²Griewank, A., and Walther, A., Evaluating Derivatives: Principles and Techniques of Algorithmic Differentiation. *Other Titles in Applied Mathematics*, SIAM, 9780898716597., (2008).

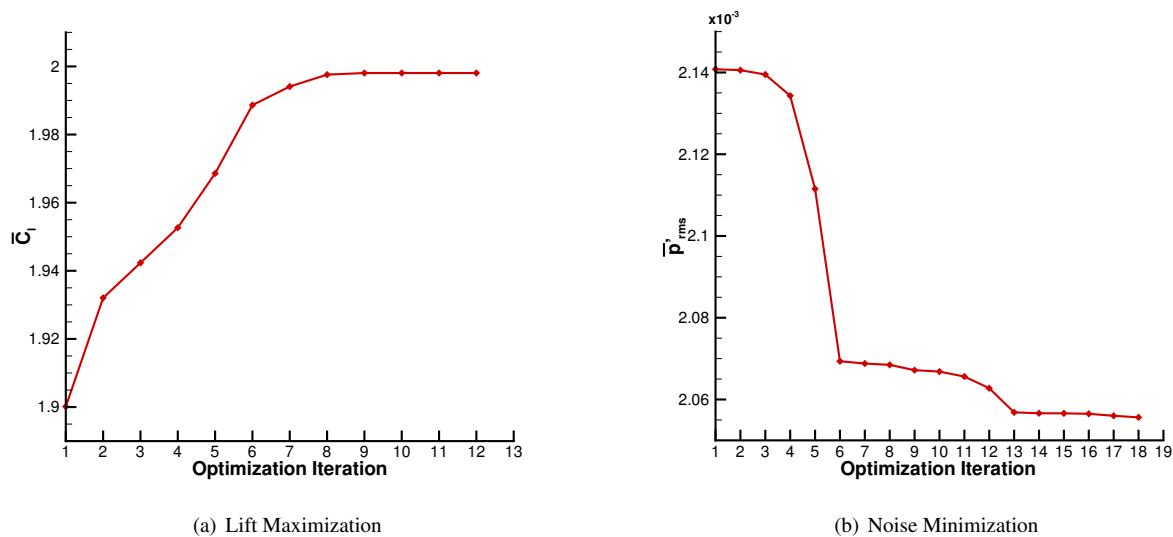


Figure 17. Optimization history of the lift maximization and noise minimization cases of the NLR7301 wing-flap geometry

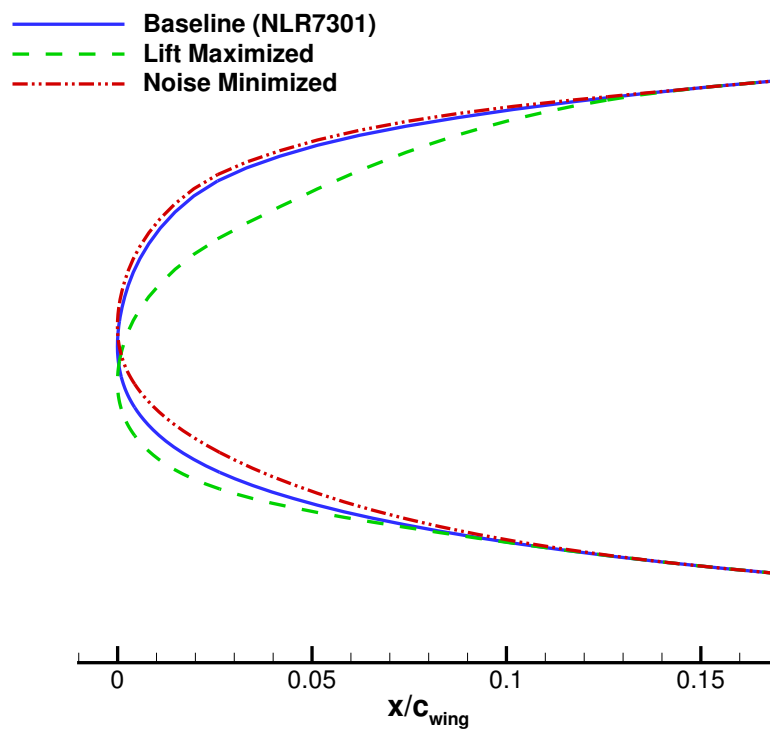


Figure 18. Comparison between the baseline (NLR7301), lift maximized and noise minimized designs in the nose region

²³Nemili, A., Özkaya, E., Gauger, N. Carnarius, A., Thiele, F., Optimal Control of Unsteady Flows Using Discrete Adjoints. *AIAA Paper* 2011-3720, (2011)